Chaos, Solitons & Fractals 54 (2013) 135–149

Contents lists available at ScienceDirect

Chaos, Solitons & Fractals

Nonlinear Science, and Nonequilibrium and Complex Phenomena

journal homepage: www.elsevier.com/locate/chaos

Multiscale analysis of depth images from natural scenes: Scaling in the depth of the woods

Yann Chéné [a], Étienne Belin [a], David Rousseau [b], François Chapeau-Blondeau [a,*]

[a] Université d'Angers, Laboratoire d'Ingénierie des Systèmes Automatisés (LISA), 62 avenue Notre Dame du Lac, 49000 Angers, France
[b] Université de Lyon, CREATIS, CNRS UMR 5220, INSERM U1044, Université Lyon 1, INSA-Lyon, 69621 Villeurbanne, France

ARTICLE INFO

Article history:
Received 24 January 2013
Accepted 13 July 2013

ABSTRACT

We analyze an ensemble of images from outdoor natural scenes and consisting of pairs of a standard gray-level luminance image associated with a depth image of the same scene, delivered by a recently introduced low-cost sensor for joint imaging of depth and luminance. We specially focus on statistical analysis of multiscale and fractal properties in the natural images. Two methodologies are implemented for this purpose, and examining the distribution of contrast upon coarse-graining at increasing scales, and the orientationally averaged power spectrum tied to spatial frequencies. Both methodologies confirm, on another independent dataset here, the presence of fractal scale invariance in the luminance natural images, as previously reported. Both methodologies here also reveal the presence of fractal scale invariance in the novel data formed by depth images from natural scenes. The multiscale analysis is confronted on luminance images and on the novel depth images together with an analysis of their statistical correlation. The results, especially the new results on the multiscale analysis of depth images, consolidate the importance and extend the multiplicity of aspects of self-similarity and fractal scale invariance properties observable in the constitution of images from natural scenes. Such results are useful to better understanding and modeling of the (multiscale) structure of images from natural scenes, with relevance to image processing algorithms and to visual perception. The approach also contains potentialities for the fractal characterization of three-dimensional natural structures and their interaction with light.

1. Introduction

Images of natural scenes are important information carrying entities [1–5]. They form the basis on which are implemented many technological image processing operations, as well as natural information processing operations as performed by the brain in visual perception. It is therefore useful to gain deeper understanding of the constitution, structures and properties of images of natural scenes. This is relevant to better modeling or synthesis of images, to better design of image processing algorithms, and also to better understanding of visual perception [4,6–11]. Visual perception and the remarkable capabilities of the brain for image processing have essentially been shaped and optimized, throughout evolution and development, in the interaction with images of natural scenes [12–18]. Understanding their constitution and properties thereof can thus shed light on operating principles at work in visual perception and useful for image processing and computational vision.

Among important generic characteristics which have been reported for images of natural scenes, is their fractal multiscale organization, manifesting regularity of constitution across scales under various forms [19–23]. Self-similarity and scale invariance properties have been reported in the spatial organization of gray-level luminance natural images. This is manifested by scale-free power-law evolutions present in the frequency spectrum of luminance images or also in their spatial correlation functions

* Corresponding author.
E-mail address: chapeau@univ-angers.fr (F. Chapeau-Blondeau).

0960-0779/$ - see front matter © 2013 Elsevier Ltd. All rights reserved.
http://dx.doi.org/10.1016/j.chaos.2013.07.007

[20,24–31]. Such scale-invariant features have also been found to exist in the temporal organization of time varying sequences of natural images, as perceived by the visual system [32]. Also, the colorimetric organization of natural images has recently been reported to carry self-similarity and fractal properties [33–36]. Such regularities across scales observed in various properties of natural images have been related to constitutive structures and details occurring uniformly over broad ranges of scales in natural scenes, with objects of many sizes, edges, occlusions, colors and shades appearing over wide ranges of depths, magnifications and lighting conditions [20,37,30]. Such fractal scaling properties observed in natural images then constitute important guides for the modeling of these images [38,8,39,40]. Also, for visual perception, this could suggest, as a design principle for optimal performance, that the visual system should distribute its capabilities uniformly in a self-similar way over a broad range of operating scales, rather than concentrating them in a narrowly focused range.

In this paper we will investigate another sector where fractal properties will be observed in images from natural scenes. We will consider depth images where the scalar intensity at each pixel gives the distance (the depth) between the camera plane and the forefront object of the scene in this spot. Such depth images have recently become easily accessible thanks to new cameras initially developed for videogames. This is the case with the Kinect imaging sensor recently released by Microsoft [41], which incorporates a standard RGB camera associated with a depth camera. A structured infrared laser light carrying a pattern of random dots is deformed by the scene and serves to construct the depth image. There is no need for any mechanical scanning of the laser thus allowing very fast acquisition of depth images, typically at a rate of 30 frames per second. This results in a low-cost fast sensor making readily accessible depth images which can be useful, outside videogames, to many scientific applications and investigations [42,43,41,44–49]. Here, we will show the potential of such depth images to contribute to the analysis of the statistics and fractal properties of images from natural scenes. The analysis we undertake will show that depth images from natural scenes also exhibit self-similarity and scale invariance properties.

In the present study, we will consider a dataset formed by an ensemble of depth images coregistered with gray-level luminance images. Two methodologies will be implemented on our dataset for scaling analysis in images, reproducing those that were employed in [26,27] on standard gray-level luminance images. The first methodology analyzes the distribution of contrasts in the images and its variation upon coarse-graining at increasing scales. This approach relates to first-order or one-point statistics of the distribution of intensities over the images. The second methodology analyzes the orientationally averaged frequency spectrum from images and its variation with frequency tied to spatial scales. This approach relates to second-order or two-point statistics characterizing the spatial arrangements of intensities over the images. These two methodologies will be applied here for the first time to the multiscale analysis of depth images. This will form the main original contribution of this paper, to report the first multiscale analysis on *depth* images from natural scenes, and to disclose and analyze the scaling properties that are observed. Beforehand, the two methodologies will be applied first to the luminance images of our dataset. This is especially useful to several purposes: (i) to confirm on another independent dataset the scaling behaviors previously reported in luminance images [26,27,20]; (ii) to validate the implementation of the multiscale analysis methodologies on standard reference (luminance) images before applying them to the new depth images; (iii) to allow for a comparison with the scaling behaviors to be observed on the new depth images. Next, the multiscale analyses applied to depth images are novel here. The outcome of the analyses will be confronted on depth images and on luminance images together with an analysis of their statistical correlation.

2. Ensemble of natural images

References [26,27] studied self-similarity and scale invariance from an ensemble of outdoor natural images taken in the woods of Hacklebarney State Park in central New Jersey, USA. Here, we analyze a comparable ensemble of natural images taken in the woods of Brain sur Longuenée in the Department of Maine-et-Loire, France. For each outdoor scene, we collected both a standard RGB image and the corresponding depth image, while the previous ensemble of [26,27] contained only standard RGB images. The images from our ensemble (both RGB and depth images) are of size 640×480 pixels, while those of [26,27] are 256×256 pixels. Fig. 1 depicts some typical examples from our ensemble of images.

The sensor [41,48,49] provides depth images with a precision in depth of around 1 cm, and the depth range covered is between 50 cm (closest distance measured by the sensor) and 550 cm (remotest distance measured by the sensor). The angular field of view is $58^\circ \times 45^\circ$ and the focal length 6 mm. In our ensemble of outdoor natural images illustrated in Fig. 1, the foreground of the scene was controlled to always lie beyond the closest 50 cm measurable distance. The points lying beyond the remotest 550 cm distance, or some points with a highly diffractive or absorbing behavior, will usually not reflect enough laser light to return a depth measurement, and such points are represented as white pixels in Fig. 1 and excluded from the subsequent statistics, following a common procedure in the processing of depth or range images [50,51]. The depth range that is resolved is of the order of $(550 - 50)/1 = 500 \approx 512$ and accordingly the depth information delivered by the sensor is codable as a nine-bit value. For the depth image, this is a little better yet comparable to the eight-bit gray-level information accessible with a standard luminance image, or with each of the three planes of a standard RGB image, as those used in [26,27].

The ensemble of [26,27] consisted of 45 standard RGB images, while our ensemble consists of 45 pairs of a standard RGB image and coregistered depth image. Here as in [26,27], when needed, the RGB image is converted into a

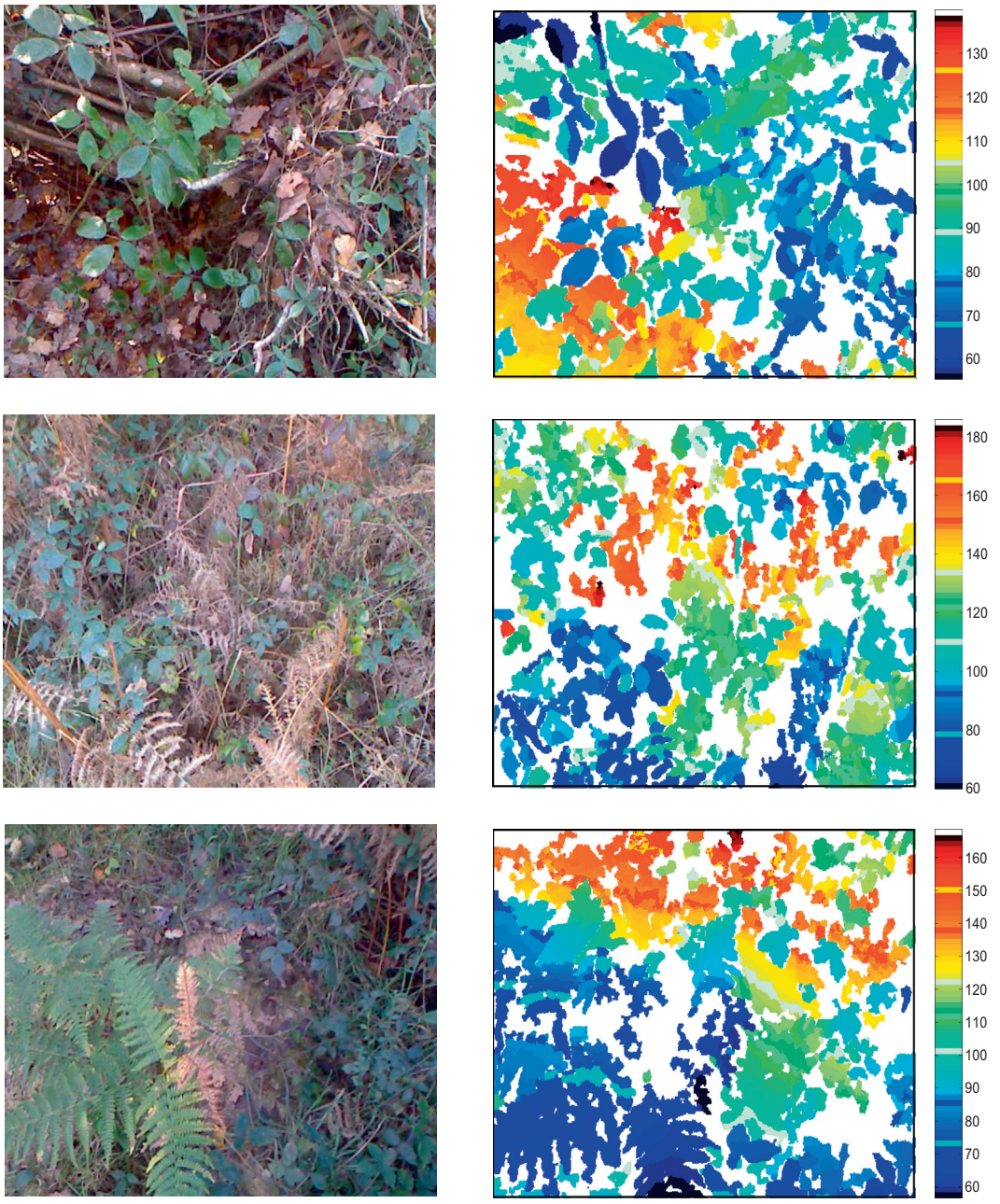

Fig. 1. Three typical examples from our ensemble of natural images, with for each of the three outdoor scenes, a standard RGB image (left) and the corresponding depth image (right).

gray-level image by computing the standard CIE luminance as $Y = 0.30R + 0.59G + 0.11B$.

3. Contrast analysis

3.1. Contrast distribution

To report self-similarity and scale invariance, Refs. [26,27] investigate the behavior of the distribution of gray levels or contrasts of an image $I(\mathbf{x})$ at pixels $\mathbf{x}$. The statistical properties are first characterized by means of the histogram $P_1(I)$ of the contrasts I. A viewpoint across scales is then obtained by considering coarse-grained images constructed by aggregation through averaging $I(\mathbf{x})$ over non-overlapping blocks of given size $N \times N$. At each aggregation scale N, the contrast I is also renormalized to zero mean and unit variance. The contrast histograms $P_N(I)$ are then compared at each scale N. Exact scale invariance holds when all the histograms $P_N(I)$ superpose at all N.

Upon such aggregation process, some useful reference behaviors can be assigned to simple image models of elementary constitutions, as illustrated in Fig. 2. For instance,

scale invariance trivially occurs when the contrasts over the image $I(\mathbf{x})$ are Gaussian and independent at each pixel $\mathbf{x}$, as illustrated in Fig. 2(top). Also, scale invariance usually breaks down with non-Gaussian contrasts on $I(\mathbf{x})$, or with spatial dependence between pixels as induced by structures or objects with a few definite sizes in the images. This is manifested in the aggregation by the successive histograms $P_N(I)$ which do not superpose. This is illustrated with a non-Gaussian mixture of contrasts resulting from two different Gaussian distributions in Fig. 2middle), and with a (non-Gaussian) uniform distribution in Fig. 2(bottom). Natural images, having more elaborate structures, often display non-Gaussian contrasts, with dependence between pixels, yet with scale invariance, as reported in Refs. [26,27] on standard gray-level luminance images from natural scenes.

For a statistical characterization of our ensemble of natural outdoor images, we further proceed as done in [26,27], by averaging the contrast histograms $P_N(I)$ over the 45 images of our ensemble, so as to obtain the ensemble-averaged histogram $\overline{P}_N(I)$ characterizing the distribution of contrasts over the ensemble.

For multiscale analysis of luminance natural images, Refs. [26,27], instead of directly operating on the original gray levels of an image $I(\mathbf{x})$, define at each pixel $\mathbf{x}$ a local contrast $\phi(\mathbf{x})$ as

$$\phi(\mathbf{x}) = \ln\left[\frac{I(\mathbf{x})}{I_0}\right], \tag{1}$$

with the constant I_0 for each image chosen so that the spatially averaged contrast $\langle\phi(\mathbf{x})\rangle$ is zero. The local contrast $\phi(\mathbf{x})$ of Eq. (1) is especially insensitive to any overall uniform change over the image, and also Ref. [27] finds that "the use of ϕ instead of I also seems to improve the observed invariances" (page 524). The statistical properties are then characterized in [26,27] by means of the histogram $P_1(\phi)$ of the luminance contrasts ϕ, and the successive histograms $P_N(\phi)$ resulting from aggregation of the contrasts ϕ over blocks of size $N \times N$ with renormalization to zero mean and unit variance at each N. Fig. 3A represents the ensemble-averaged distribution $\overline{P}_N(\phi)$ for the contrast ϕ according to Eq. (1), when the image $I(\mathbf{x})$ is a gray-level luminance image computed for an outdoor natural scene as in Fig. 1left). In addition to the ensemble average of Fig. 3A, in order to appreciate the variability over the ensemble, Fig. 3B shows a representative configuration with error bars evaluated over the 45 images of the ensemble.

For the luminance natural images, the distribution of contrast in Fig. 3 is found essentially similar at the various scales N, and is also non-Gaussian. This manifests scale invariance in the luminance natural images from our ensemble. Scale invariance was also observed, with the same methodology, in the ensemble of luminance natural images of [26,27]. This confirms the tendency of luminance images from natural scenes to stand as complex information-carrying structures, displaying dependencies between pixels and non-Gaussian distributions of contrast incorporating self-similarity across scales.

Next, we are now in a position to apply the same multiscale characterization, for the first time to depth images of natural scenes as provided by our ensemble, when the contrast $I(\mathbf{x})$ at each pixel $\mathbf{x}$ is the depth of the scene at this location. When $I(\mathbf{x})$ is a depth image of an outdoor natural scene as in Fig. 1right), we show in Fig. 4A the ensemble-averaged distribution $\overline{P}_N(I)$ characterizing the depths over the images of our dataset. In addition to the ensemble average of Fig. 4A, to appreciate the variability, Fig. 4B shows a representative configuration with error bars evaluated over the 45 images of the ensemble.

For the depth images of natural scenes, the distribution of contrast in Fig. 4 is also found essentially self-similar at the various scales N. The self-similar evolution displays slightly more pronounced variability over the ensemble for the depth images, as manifested by slightly larger error bars in Fig. 4B, compared to the luminance from Fig. 3B. This can be related to a lesser number of points available for the depth statistics due to some excluded points not returning enough light for a depth measurement, as explained in Section 2. The overall self-similar behavior in Fig. 4 demonstrates that scale invariance in natural scenes also extends to new types of spatial measurements such as the depth images. Therefore, depth images from natural scenes also appear as complex information-carrying structures, with dependencies between pixels (as confirmed by the power spectrum to come in Section 4) and with distributions of contrast incorporating self-similarity across scales.

Confrontation of Figs. 3 and 4 shows that the contrasts in luminance and in depth display in common a scale-invariant distribution, although in their detail these distributions differ between luminance and depth images. This difference is not unexpected, since the physical information carried by each type of images, namely luminance or depth, is essentially distinct. In this respect, it can be noted that the distribution of contrasts for the luminance images of Fig. 3 is scale-invariant and non-Gaussian, and essentially departs from Gaussianity for the small contrasts which are found more probable than with a Gaussian distribution. This reveals that natural images tend to be dominated by small variations of gray levels of luminance, presumably associated with the slight variations of shades of an otherwise uniform gray that would generally characterize each coherent object or structure present in natural scenes. And this type of distribution appears as scale-invariant for the gray levels. Meanwhile, the distribution of depths in the images of Fig. 4 is scale-invariant and non-Gaussian, and essentially departs from Gaussianity for the large depths which are found more probable than with a Gaussian distribution. This can also be understood as a mark of the coherent objects or structures present in natural scenes, which are in general sufficiently separated in space in a way which makes rather frequent large variations in depth, however scale-invariant. The complex spatial organization of natural scenes, with structures and details present over broad ranges of scales, is thus manifested and recordable from luminance images as well as from depth images.

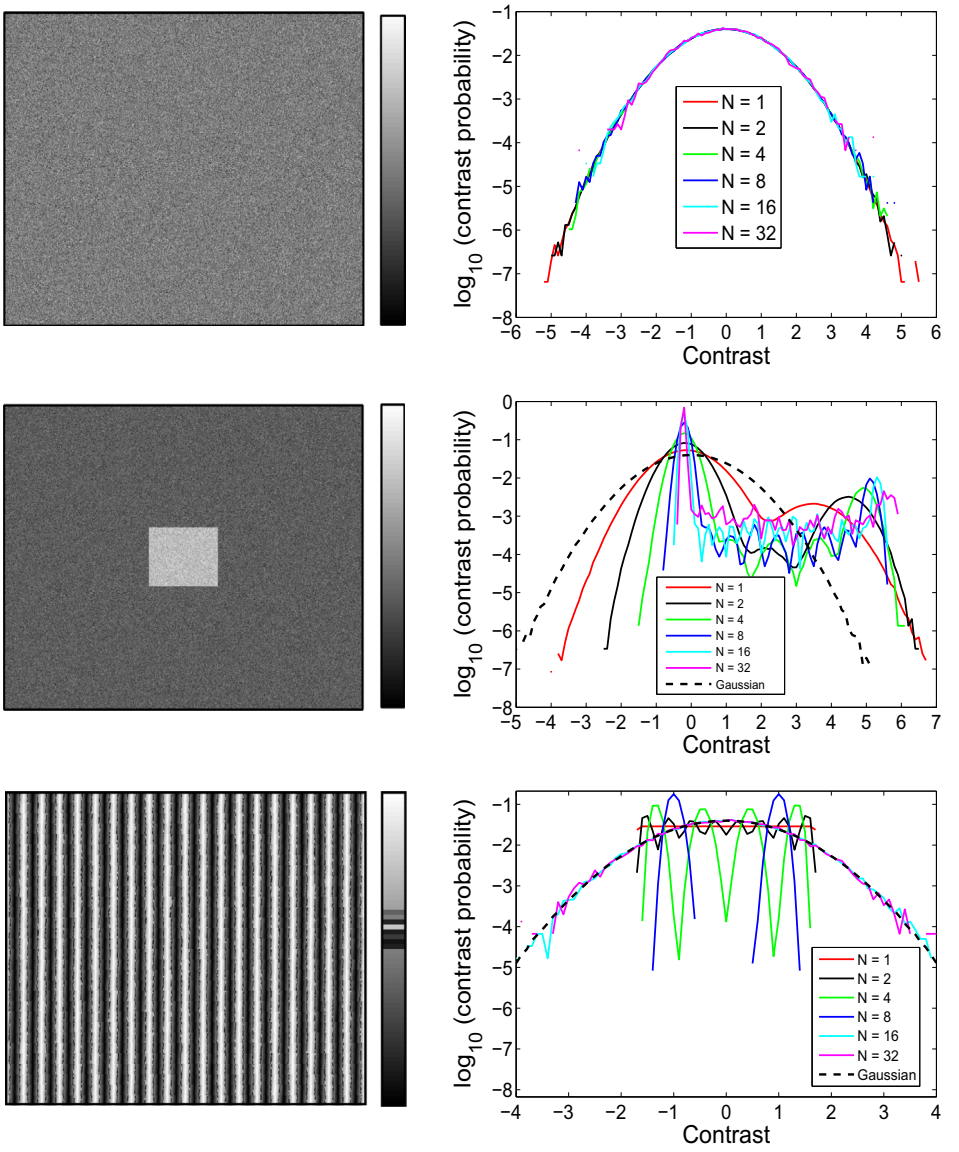

Fig. 2. Three examples of reference images $I(\mathbf{x})$ with simple spatial constitutions (left) and associated histograms $P_N(I)$ of the gray levels I upon aggregation over blocks of size $N \times N$ pixels and renormalization to zero mean and unit variance (right): (top) a purely random image with no spatial structure (white noise) and Gaussian gray levels showing exact scale invariance; (middle) a bright object on a dark background both having narrow quasi non-overlapping random distributions of gray levels and no scale invariance; (bottom) an image with uniform distribution of gray levels and regular spatial modulation and no scale invariance. The dashed lines depict theoretical Gaussian distributions.

3.2. Gradient of contrast

For further investigation of spatial self-similarity and scale invariance, Refs. [26,27] consider the gradient $\nabla I(\mathbf{x})$ of the image $I(\mathbf{x})$, and its evolution with the aggregation scale N. At every scale N, the image $I(\mathbf{x})$ undergoes the aggregation process over blocks of size $N \times N$ followed by the renormalization to zero mean and unit variance, as implemented in Section 3.1. The ensuing gradient $\nabla I(\mathbf{x})$ has a magnitude $|\nabla I|$ which provides a local scalar, whose distribution is analyzed according to the aggregation scale N.

For simple reference images $I(\mathbf{x})$ as in Fig. 2, the distribution of magnitude of the gradient $|\nabla I|$ is presented in Fig. 5. The Gaussian random image of Fig. 5(top) is an example showing exact scale invariance of the magnitude of the gradient $|\nabla I|$. As visible in Fig. 5(top), the distributions of magnitude of the gradient $|\nabla I|$ superpose at every scale N, and they follow a Rayleigh distribution when the image $I(\mathbf{x})$ is Gaussian [26,27]. On the contrary, for images incorporating non-Gaussian gray levels associated with simple spatial structures with a few definite scales, such as in Fig. 5middle)-(bottom), no scale invariance is detected with the distributions of magnitude of the gradient $|\nabla I|$ differing according to the scale N. Natural images, having more elaborate structures, usually display specifically balanced distributions of small and large magnitudes of gradient, are non-Rayleigh, yet tend to be invariant across

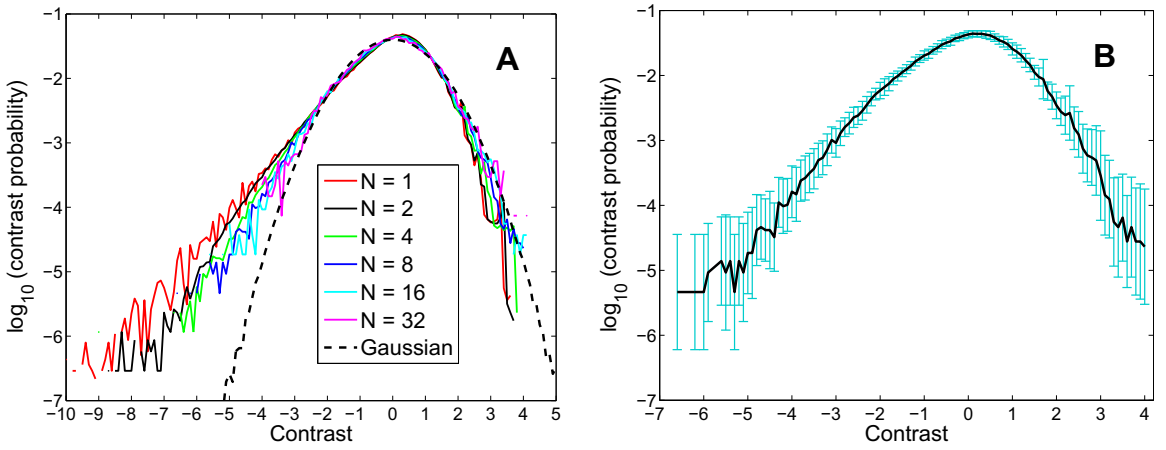

Fig. 3. Distributions $\overline{P}_N(\phi)$ of luminance contrast ϕ according to Eq. (1) when the image $I(\mathbf{x})$ is a standard gray-level luminance image of an outdoor natural scene as in Fig. 1 (left). (A): The different curves (solid lines) show the distributions obtained by averaging the contrasts ϕ over $N \times N$ pixel blocks and renormalization to zero mean and unit variance, for various N (solid lines). The distributions appear scale-invariant and non-Gaussian. (B): The configuration $N = 8$ with error bars at plus and minus one standard deviation evaluated over the 45 luminance images of the ensemble.

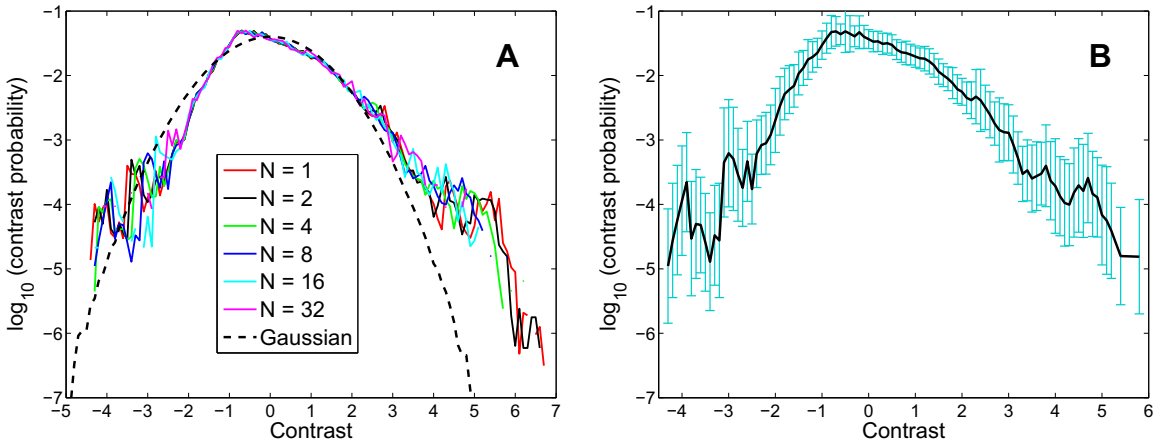

Fig. 4. Distribution $\overline{P}_N(I)$ of depth contrast when the image $I(\mathbf{x})$ is a depth image of an outdoor natural scene as in Fig. 1 (right). (A): The different curves (solid lines) show the distributions obtained by averaging the depths I over $N \times N$ pixel blocks and renormalization to zero mean and unit variance, for various N. The distributions appear scale-invariant and non-Gaussian. (B): The configuration $N = 8$ with error bars at plus and minus one standard deviation evaluated over the 45 depth images of the ensemble.

spatial scales, as reported in Refs. [26,27] on standard gray-level luminance images from natural scenes.

For statistical characterization of our ensemble of natural images, we further proceed as done in [26,27], by averaging the distribution of magnitude of the gradient $|\nabla I|$ over the 45 images of our ensemble. For the analysis of the gradient in luminance also, Refs. [26,27] instead of directly operating on an original luminance image $I(\mathbf{x})$ find it more appropriate to operate on the contrast image $\phi(\mathbf{x})$ from Eq. (1). The resulting ensemble-averaged distribution of $|\nabla\phi|$ characterizing the ensemble is presented in Fig. 6A for the standard gray-level luminance images as in Fig. 1left), together with an illustration of the variability over the ensemble presented in Fig. 6B.

For the luminance natural images, the distribution of magnitude of the gradient $|\nabla\phi|$ in Fig. 6 displays a behavior similar to that of the images from [26,27]. There is an overall invariant form of the distribution of the gradient with the scale N. This distribution, although scale-invariant, significantly departs from the Rayleigh form that prevails in a Gaussian world; and instead this distribution shows an essentially exponential tail. These properties are observed in common here and in [26,27], and constitute another manifestation of elaborate scale-invariant structures present in outdoor natural images.

Next, we are in a position to apply for the first time this multiscale analysis of the gradient when $I(\mathbf{x})$ is a depth image from our ensemble as in Fig. 1right). In such condition, Fig. 7A represents the ensemble-averaged distribution of magnitude $|\nabla I|$ of the gradient for the depth images of our ensemble as in Fig. 1right), with the variability over the ensemble illustrated in Fig. 7B.

The evolution curves of $|\nabla I|$ at the various scales N in Fig. 7 have been translated in their ordinates to show that in most part of their tail these curves tend to superpose. Only at very small values of the gradient $|\nabla I|$ are some sig-

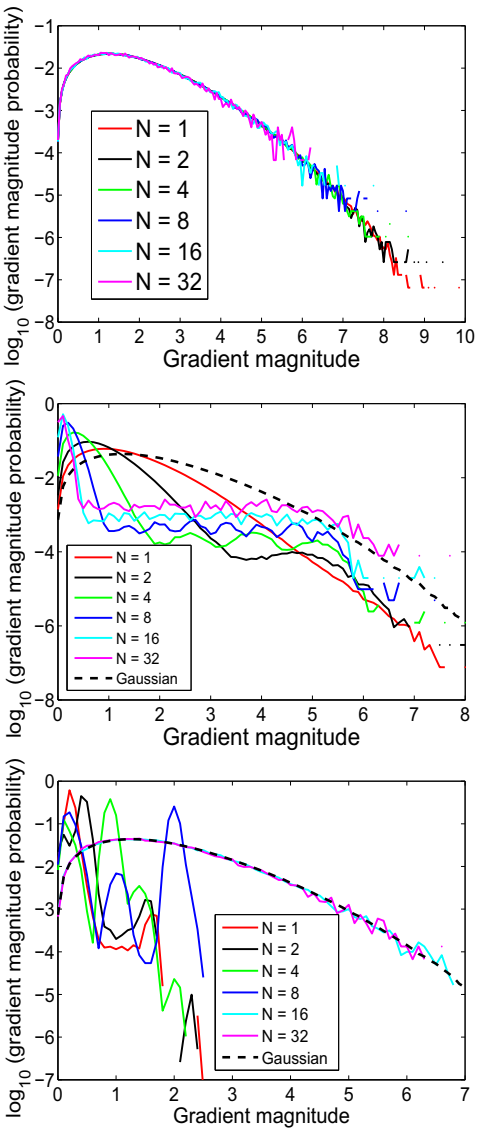

Fig. 5. For the same three reference images $I(\mathbf{x})$ as in Fig. 2 in the same top-down order, the histograms of magnitude of the gradient $|\nabla I|$ upon aggregation of $I(\mathbf{x})$ over blocks of size $N \times N$ and renormalization to zero mean and unit variance: (top) purely random image with no spatial structure (white noise) and Gaussian gray levels showing exact scale invariance and a Rayleigh distribution for $|\nabla I|$; (middle) bright object on a dark background both having narrow quasi non-overlapping random distributions of gray levels and no scale invariance in the distribution of $|\nabla I|$; (bottom) image with uniform distribution of gray levels and regular spatial modulation and no scale invariance in the distribution of $|\nabla I|$. The dashed lines depict the theoretical Rayleigh distribution of $|\nabla I|$ associated with a Gaussian gray-level contrast $I(\mathbf{x})$.

nificant differences observable in the distributions at distinct scales N in Fig. 7. At small N, neighboring pixels are expected with high probability to show similar contrasts, whence the high probability of small gradient $|\nabla I|$, which can be attributed to coherent structures or objects existing in the scene. Through aggregation at larger N, coherent objects gradually mix, leading to neighboring pixels with more heterogeneous contrasts, and less probability of small gradient $|\nabla I|$. This distinctive behavior with N only concerns very small gradients $|\nabla I|$ in Fig. 7. Above very small gradients $|\nabla I|$ in Fig. 7, the distributions of $\nabla I|$ tend to superpose at various N, manifesting scale invariance of the distribution of $|\nabla I|$, except for very small $|\nabla I|$.

For the depth images, the distribution of magnitude of the gradient in Fig. 7, in addition to displaying self-similarity across scales, is also found to strongly depart from the Rayleigh distribution prevailing in a Gaussian world. This demonstrates that the gradient distribution also reflects nontrivial scale invariance in the new type of spatial measurements formed by the depth images. There is therefore a strong parallel between luminance and depth images from natural scenes, which both incorporate scale invariance, detectable at the same time in their distributions of contrast and of gradients.

4. Spectrum analysis

As another approach to report scale invariance and fractal properties, Refs. [26,27] consider the power spectrum for the images. The power spectrum of an image $I(\mathbf{x})$ is computed in [26,27] via the periodogram method, through the squared modulus of the two-dimensional Fourier transform,

$$\mathcal{I}(\rho,\theta) = |\mathrm{FT}[I(\mathbf{x})]|^2 \tag{2}$$

expressed in polar coordinates in the plane of spatial frequencies. An average is then performed over the angular coordinate θ to yield the orientationally averaged spectrum

$$\overline{\mathcal{I}}(\rho) = \frac{1}{2\pi}\int_0^{2\pi} \mathcal{I}(\rho,\theta)d\theta. \tag{3}$$

Scale invariance or self-similarity over scale is manifested by an average spectrum $\overline{\mathcal{I}}(\rho)$ displaying a scale-free power-law evolution of the form $\overline{\mathcal{I}}(\rho) = A\rho^a$, with a negative exponent a for the decay of the spectrum with increasing spatial frequencies ρ.

Upon such spectral characterization, some useful reference behaviors can be assigned to simple image models with elementary constitutions, as illustrated in Fig. 8. For instance, scale invariance trivially occurs for a purely random image (white noise) with no spatial structure, as shown in Fig. 8(top). The resulting power spectrum $\overline{\mathcal{I}}(\rho)$ from Eqs. (2) and (3) is flat following a degenerate power law $\overline{\mathcal{I}}(\rho) = A\rho^a$ with exponent $a = 0$, manifesting the trivial scale invariance of the white noise image with no spatial structure. Scale invariance breaks down for instance when a simple low-pass filtering is implemented on the white noise image, as illustrated in Fig. 8middle). The low-pass filter induces correlation of the gray levels, over a spatial range determined by the size of the convolution kernel associated with the filter. A two-dimensional triangular kernel (a pyramid) of base size 21×21 pixels was used in Fig. 8middle). The corresponding power spectrum $\overline{\mathcal{I}}(\rho)$ clearly departs from a uniform power law, with a cut-off frequency determined by the correlation length of the filter which introduces a specific spatial scale in the filtered image no longer invariant. Next, an object with definite spatial dimensions well contrasted over a background, as in

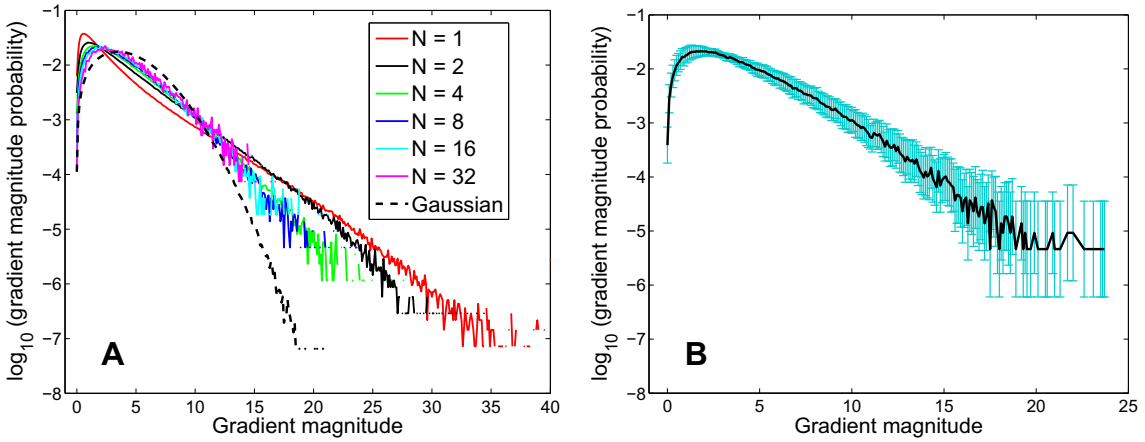

Fig. 6. Distribution of the magnitude of the gradient $|\nabla\phi|$ for the luminance contrast $\phi(\mathbf{x})$ from Eq. (1) when the image $I(\mathbf{x})$ is a standard gray-level luminance image of an outdoor natural scene as in Fig. 1 (left). (A): The different curves (solid lines) show the distributions obtained after averaging the contrasts ϕ over $N \times N$ pixel blocks and renormalization to zero mean and unit variance, for various N. The dashed line depicts the theoretical Rayleigh distribution of $|\nabla\phi|$ associated with a Gaussian contrast $\phi(\mathbf{x})$. (B): The configuration $N = 8$ with error bars at plus and minus one standard deviation evaluated over the 45 luminance images of the ensemble.

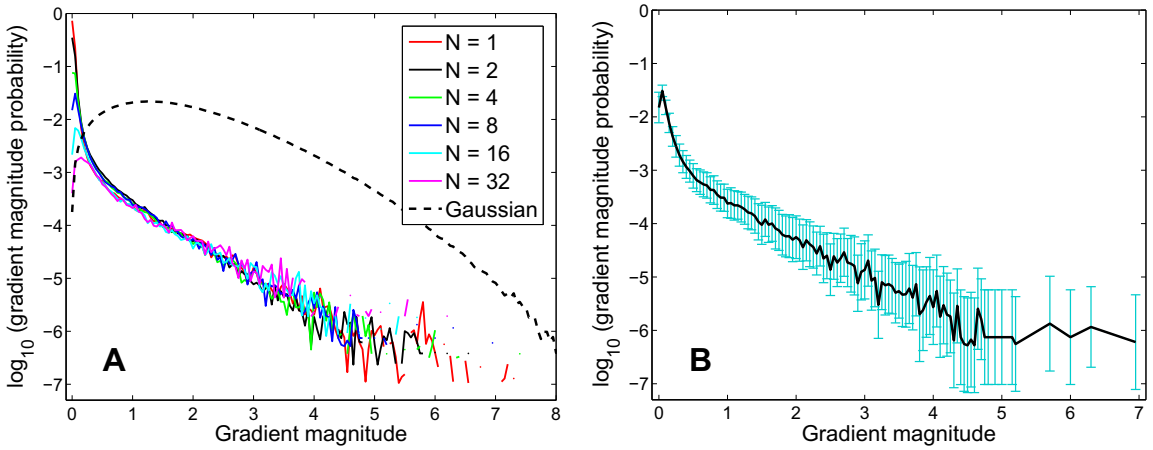

Fig. 7. Distribution of the magnitude of the gradient $|\nabla I|$ when the image $I(\mathbf{x})$ is a depth image of an outdoor natural scene as in Fig. 1 (right). (A): The different curves show the distributions obtained after averaging the depths I over $N \times N$ pixel blocks and renormalization to zero mean and unit variance, for various N. The dashed line depicts the theoretical Rayleigh distribution of $|\nabla I|$ associated with a Gaussian depth image $I(\mathbf{x})$. (B): The configuration $N = 8$ with error bars at plus and minus one standard deviation evaluated over the 45 depth images of the ensemble.

the image of Fig. 8(bottom), displays a power spectrum $\overline{\mathcal{I}}(\rho)$ departing from a uniform power law, but with lobes or features reflecting the typical spatial sizes in the object. Such a power spectrum manifests the existence of a few well determined spatial scales dominating the image which has no scale invariance. Especially, in such non-scale-invariant images, the power spectrum $\overline{\mathcal{I}}(\rho)$ at low spatial frequencies ρ tends to return to the flat spectrum of the white noise. This indicates that there exists in the image a characteristic spatial scale (related to a cut-off frequency) beyond which the gray levels tend to vary independently, as for a white noise. By contrast, scale-invariant images do not contain such characteristic spatial scales. This is indicated by a power spectrum following a nontrivial power law $\overline{\mathcal{I}}(\rho) \sim \rho^{a}$, with $a \neq 0$, especially in the low-frequency end, associated with long-range spatial correlation maintained in the variations of the gray levels, as a mark of an elaborate constitution. Natural images often display such behavior, where no dominant scales in a small number single out, but instead where a broad range of scales are uniformly represented. This usually leads to scale-free power-law evolution of the power spectrum $\overline{\mathcal{I}}(\rho)$ as reported in Refs. [26,27] on standard gray-level luminance images from natural scenes.

For a statistical characterization of our ensemble of natural outdoor images, we further proceed as done in [26,27], by averaging the power spectrum $\overline{\mathcal{I}}(\rho)$ from Eqs. (2) and (3) over the 45 images of our ensemble, so as to obtain the ensemble-averaged power spectrum characteristic of the ensemble.

As in the luminance contrast analysis of Section 3, for the analysis of the power spectrum, Refs. [26,27] instead of directly operating on an original luminance image $I(\mathbf{x})$ in Eq. (2), operate on the contrast image $\phi(\mathbf{x})$ from Eq.

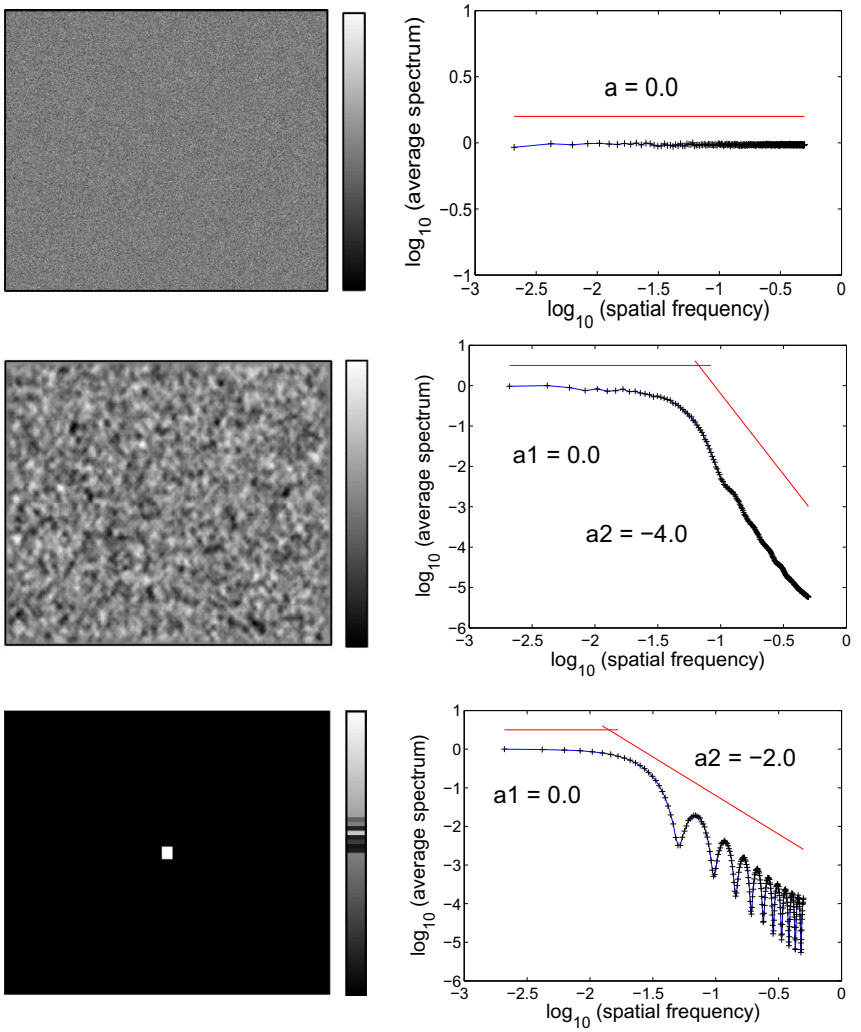

Fig. 8. Three examples of reference images $I(\mathbf{x})$ with simple spatial constitutions (left) and associated average power spectra $\overline{\mathcal{I}}(\rho)$ (right): (top) a purely random image with no spatial structure (white noise) and flat spectrum with power-law exponent $a = 0$; (middle) a random image with short-range spatial correlation and spectrum with a frequency cut-off controlled by the correlation length in space, and two power-law exponents $a = 0$ and $a = -4$ on both sides of the cut-off; (bottom) a uniform object on a uniform background and spectrum with lobes reflecting the typical spatial sizes in the object. The two slopes $a = 0$ and $a = -2$ are controlled by the sinc squared function theoretically modeling this spectrum.

(1), to obtain from Eqs. (2) and (3) an orientationally averaged spectrum denoted $\overline{\Phi}(\rho)$. In this condition, Fig. 9 represents the ensemble-averaged power spectrum obtained from the luminance images as in Fig. 1left) of our ensemble of outdoor natural scenes.

For the luminance natural images, the power spectrum in the log–log plot of Fig. 9 is well approximated by a power law ρ^a with a non-integer fractal exponent $a = -1.83$, over a large range of the spatial frequency ρ extending especially in the low-frequency end. The power law is the mark of scale-free self-similar long-range spatial correlation associated with the low-frequency end of the spectrum. An identical behavior is reported for the power spectrum of the ensemble of luminance natural images considered in [26,27], especially with a very close fractal exponent $a = -1.83$ in [26,27]. Also, in the power spectrum of Fig. 9 there is a cut-off in the high-frequency range to a steeper power law ρ^a with exponent $a = -4.62$. The same cut-off is also observed in [26,27], to a steeper exponent $a = -4.16$. This effect can be assigned to high-frequency noise superposing to low-frequency correlation present in the images, both from our ensemble and from that of [26,27] in a consistent way. This confirms the tendency of luminance images from natural scenes to carry long-range scale-invariant dependencies in their spatial organization.

Next, we apply the power spectrum analysis for the first time to depth images from outdoor natural scenes. Fig. 10 represents the ensemble-averaged power spectrum obtained from the depth images as in Fig. 1right) of our ensemble of outdoor natural scenes.

For the depth images of natural scenes, the power spectrum of Fig. 10 is well approximated by a power law ρ^a with a non-integer fractal exponent $a = -2.20$, over almost

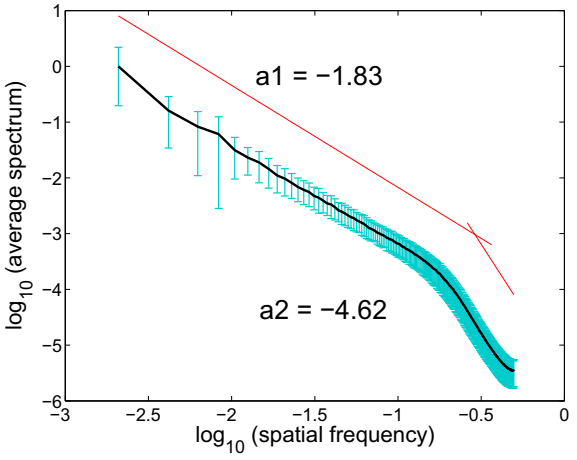

Fig. 9. From the contrast image $\phi(\mathbf{x})$ from Eq. (1), power spectrum $\overline{\Phi}(\rho)$ from Eqs. (2) and (3) averaged over the ensemble of luminance images of outdoor natural scenes as in Fig. 1 (left). The scale-free power law ρ^a with non-integer fractal exponent $a = -1.83$ provides a good model over most of the spatial frequencies ρ accessible, especially in the low-frequency end associated with long-range spatial correlation in the luminance images. The error bars at plus and minus one standard deviation are evaluated over the 45 luminance images of the ensemble.

the whole range accessible for the spatial frequency ρ. This demonstrates that long-range scale-free correlations are also present in the new type of spatial measurements formed by the depth images. Long-range scale-free spatial dependencies are thus manifested and recordable in depth images as well as in luminance images from natural scenes. The specific values of the exponent of the scale-free power-law spectra from luminance images (Fig. 9) or from depth images (Fig. 10) are however distinct. Again, this is not unexpected, since the luminance or depth information carried by each type of images are essentially distinct. We investigate further in the next section the possible relation between luminance and depth images.

5. Relation between luminance and depth images

In this study we did not make any assumption on the possible correlation or relation between luminance and depth images. Instead, we implemented independent parallel analyses of the scaling properties of luminance and of depth images. Any conceivable correlation between the two types of images is expected to critically depend on the lighting conditions. External lighting in the visible range, through its intensity and orientation, strongly affects the luminance images; but it leaves unaffected the depth images. Lowering the external lighting to extinction can completely wipe out any correlation between luminance and depth images. So any relation between these two may only be of statistical nature in given lighting conditions. For instance, in standard day-light conditions, Refs. [51–53] analyzed the correlation between luminance and depth images. The depth images in [51–53] were constructed with a laser scanner, a method with high accuracy and spatial range, but with a delay of minutes to scan an image, much longer than the 30 Hz image rate of our sensor here; and [51–53] did not address scaling behaviors in the images as we do here by direct analysis in the line of Refs. [26,27]. To gain further insight into the fractal scaling observed simultaneously here in luminance and in depth images, we undertook a correlation analysis between the luminance and depth images from our dataset. The cross-correlation coefficient between the luminance and corresponding depth images was evaluated as in Refs. [51,53] by

$$\rho = \frac{\langle I_{\text{lumin}}(\mathbf{x}) I_{\text{depth}}(\mathbf{x})\rangle - \langle I_{\text{lumin}}(\mathbf{x})\rangle\langle I_{\text{depth}}(\mathbf{x})\rangle}{\text{std}[I_{\text{lumin}}(\mathbf{x})]\,\text{std}[I_{\text{depth}}(\mathbf{x})]} \tag{4}$$

where $\langle\cdot\rangle$ stands as an average over the pixels of the images; and ρ was computed for each of the 45 pairs of images of our ensemble. The mean $\langle I(\mathbf{x})\rangle$ and standard deviation std$[I(\mathbf{x})]$ were also computed for all the images $I(\mathbf{x})$ of the ensemble.

To appreciate the impact of the lighting conditions, the cross-correlation ρ is plotted in Fig. 11 as a function of the mean value $\langle I_{\text{lumin}}(\mathbf{x})\rangle$ of the luminance over the 45 pairs of images of our ensemble.

In Fig. 11, the distribution of the ordinates shows that the cross-correlation coefficient ρ generally assumes relatively low values. This manifests that the overall correlation between the luminance and depth images from the same scene is in general relatively low. Moreover, in Fig. 11 the abscissas show that the mean luminance $\langle I_{\text{lumin}}(\mathbf{x})\rangle$ has usually no directed or determined influence on the cross-correlation ρ. Increasing the mean luminance does not consistently make the cross-correlation ρ larger or smaller. Such a weak relation is not unexpected for two distinct physical quantities, with the depth which is unaffected by the lighting conditions which in turn critically influence the luminance. Nevertheless, the rather weak cross-correlation ρ in Fig. 11 is very often found negative. This expresses that, most often in our dataset, as the depth increases the luminance tends to decrease. This is a

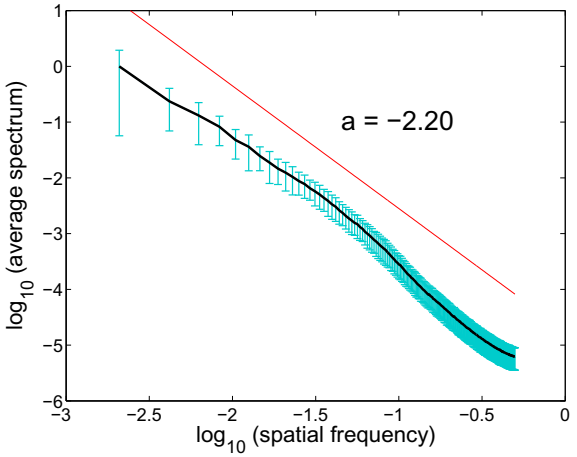

Fig. 10. From the depth image $I(\mathbf{x})$, power spectrum $\overline{\mathcal{I}}(\rho)$ from Eqs. (2) and (3) averaged over the ensemble of depth images $I(\mathbf{x})$ of outdoor natural scenes as in Fig. 1 (right). The scale-free power law ρ^a with non-integer fractal exponent $a = -2.20$ provides a good model over the spatial frequencies ρ accessible. The error bars at plus and minus one standard deviation are evaluated over the 45 depth images of the ensemble.

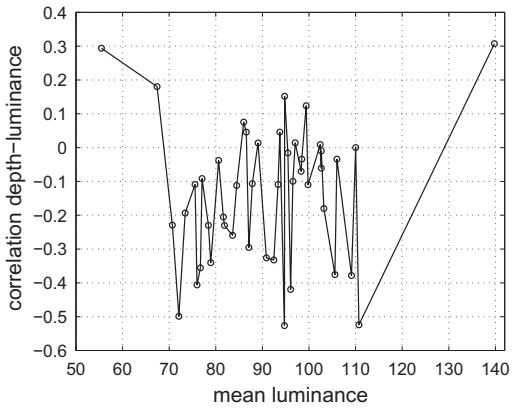

Fig. 11. Cross-correlation coefficient ρ from Eq. (4) between the luminance and corresponding depth image, as a function of the mean value $\langle I_{\text{lumin}}(\mathbf{x})\rangle$ of the luminance image, computed for the 45 pairs of images of our ensemble.

reasonable behavior for outdoor natural scenes dominated by leafy foliage, with illumination coming from outside any bush or tree, resulting usually in decreasing light by penetrating deeper into the foliage with increasing depth. These are the conditions that prevail in our ensemble of natural images, leading to mainly negative cross-correlation ρ in Fig. 11. Most of the values of the cross-correlation ρ in Fig. 11 lie in the range of -0.1 to -0.3, which matches the overall correlation in the neighborhood of -0.18 reported in [51]. Still, a few points in the graph of Fig. 11 single out with a relatively high positive cross-correlation ρ around *0.2* or *0.3*. This corresponds to images in the ensemble with a dominant illumination coming from the remote background, typically as shown in Fig. 12 with the background opening at infinity on a bright sky, leading to an illumination increasing with depth. Such a remote light source at infinity in the background returns no information for the depth images, as explained in Section 2. Consistently, most of the scenes of our ensemble of images have no such dominant illumination source visible in a remote background, but rather they rest, as in Fig. 1, in a diffuse illumination coming from the outer boundary of the foliage structures and receding while going deeper into them.

It is interesting to note that, although the level of cross-correlation ρ between luminance and depth images is generally small, its nonzero value, by its sign, can provide a hint on the structure of the dominant illumination of the scene, either coming from the background yielding positive correlation, of receding with depth yielding negative correlation.

Another viewpoint is offered by Fig. 13 which shows the cross-correlation coefficient ρ from Eq. (4) for pairs of luminance and depth images obtained from the same scene successively measured in different illuminations corresponding to different day-light conditions. In such circumstances the depth image is invariant, and the luminance image evolves with the changing illumination. The illumination which changes in intensity and orientation significantly affects the luminance image, especially through shading and light interception which occurs differently in the depth of the foliage and bushes. These changes in the luminance image induce significant changes in the cross-correlation ρ in Fig. 13. However, the cross-correlation ρ in Fig. 13 consistently remains small and mainly negative between the luminance and depth images. This is the same dominant behavior of the cross-correlation ρ as reflected by the analysis over the whole ensemble in Fig. 11.

The cross-correlation ρ of Figs. 11–13 is computed across the pixels of the images. A complementary view assesses the cross-correlation across the images of the ensemble. Such a view is provided by Fig. 14A which depicts the mean luminance $\langle I_{\text{lumin}}(\mathbf{x})\rangle$ versus the mean depth $\langle I_{\text{depth}}(\mathbf{x})\rangle$, computed for each of the 45 image pairs of our ensemble. The scattered plot of Fig. 14A shows no strong regular relation generally connecting the mean luminance and mean depth across our ensemble of natural images.

A similar picture emerges from Fig. 14B which depicts the luminance standard deviation std$[I_{\text{lumin}}(\mathbf{x})]$ versus the depth standard deviation std$[I_{\text{depth}}(\mathbf{x})]$, for each of the 45 image pairs of our ensemble. These standard deviations can be seen as measures of the overall texture over a luminance or a depth image. In a similar way, the scattered plot of Fig. 14B shows no strong regular relation connecting the standard deviations or textures in luminance and in depth across our ensemble of natural images.

It is possible to also evaluate cross-correlation coefficients between the means $\langle I(\mathbf{x})\rangle$ and standard deviations std$[I(\mathbf{x})]$ computed among the 45 luminance images and 45 depth images of our ensemble. The results are presented in Table 1, and they also consistently point to weak and negative correlations between luminance and depth images.

From these observations, it results that the luminance and depth images from our dataset are in general weakly correlated. At the same time, the independent evaluations we conducted here, showed that these two types of images exhibit in common self-similar scaling organizations. Fractal parameters have been extracted for luminance and for depth images through independent statistical analysis over the image ensemble. These fractal parameters are global parameters emerging from statistical analysis over the ensemble of images. They come out with different quantitative values for luminance and depth images, consistent with the facts that these two types of images are weakly

Fig. 12. Image with the dominant source of illumination coming from the remote background.

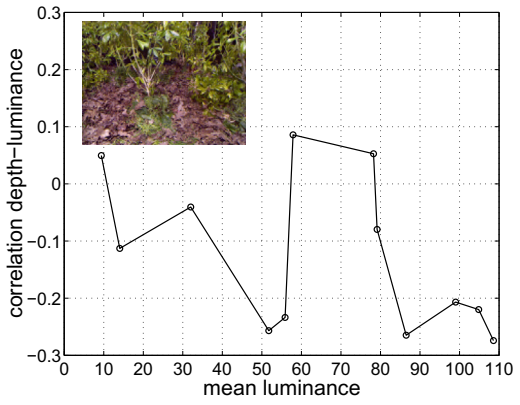

Fig. 13. Cross-correlation coefficient ρ from Eq. (4) between the luminance and corresponding depth image, as a function of the mean value $\langle I_{\text{lumin}}(\mathbf{x})\rangle$ of the luminance image, for pairs of images obtained from the same scene of the inset successively measured in different conditions of illumination.

correlated and represent two distinct physical quantities. Yet, beyond the quantitative values of the fractal parameters which differ, the qualitative property of a fractal self-similar organization is an important common trait between luminance and depth images. This points to a possible common origin resting in the constitution of the natural scenes which would encompass fractal structures and details in a self-similar way across scales. Such fractal structures in the scene would interact with the incident light, and project onto an image plane at the location of a sensing device, sensitive to luminance or to depth, so as to construct an image with distinctive properties, yet carrying a specific mark of the fractal properties of the physical scene. This leads in the images to self-similar scaling organizations which appear as high-level structural properties, not fully captured or predictable by a low-level measure of dependence like cross-correlation.

6. Discussion

We have used a newly introduced low-cost fast sensor for depth image measurement to construct an ensemble of images from outdoor natural scenes. The ensemble consisted of pairs of a standard luminance image coregistered with a depth image of the same scene. The resulting depth images render easily accessible a novel modality of imaging carrying useful potentialities for many purposes in image processing and computer vision. The depth images were used here to further explore fractal multiscale properties in images from natural scenes. As a result, we report here, for the first time to our knowledge, a multiscale analysis of depth images from natural scenes. We also confront the multiscale analysis on depth images and on luminance images. Two methodologies were implemented for the multiscale analysis, in a close parallel with Refs. [26,27] which analyzed standard gray-level luminance images from outdoor natural scenes. Our results here with both methodologies confirm, on another independent dataset, the presence of scale invariance in the luminance natural images, as already reported by Refs. [26,27] and by others [24,25,20]. Our results with both methodologies also reveal that scale invariance extends to the novel data formed by depth images from natural scenes. This is the most prominent original result of this study: to report the first multiscale analysis on depth images from natural scenes, and to disclose and analyze their scaling properties. Scale invariance is found in the distribution of contrast and of its gradient over the images, both for luminance and for depth images. The precise quantitative laws characterizing the scaling in these two types of images are distinct, as they refer to two distinct physical quantities (luminance and depth), but they have in common to share a fractal scale-invariant self-similar organization. The same is true for the fractal scale invariance found in the orientationally averaged power spectrum, which is quantitatively distinct for luminance and for depth images, but in both cases is governed by scale-free power-law evolutions with non-integer fractal exponents. These results consolidate the importance of fractal scale invariance as a generic property, detectable under multiple forms, in the constitution of images from natural scenes.

We have tested here an ensemble of outdoor natural scenes with plants, bushes and trees, this especially allowing confrontation with comparable dataset from the literature [26,27]. Ensembles of other types, with other specific typologies, could be tested to extend the investigation and

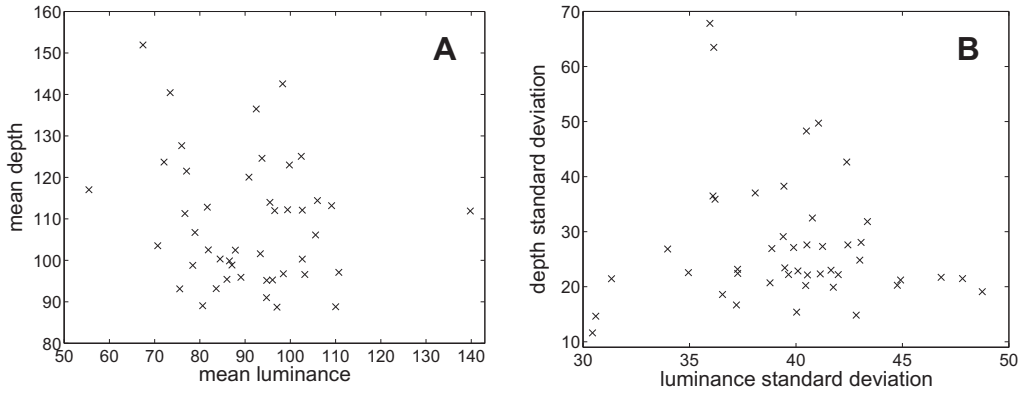

Fig. 14. (A) mean luminance $\langle I_{\text{lumin}}(\mathbf{x})\rangle$ versus mean depth $\langle I_{\text{depth}}(\mathbf{x})\rangle$, and (B) standard deviation std$[I_{\text{lumin}}(\mathbf{x})]$ versus std$[I_{\text{depth}}(\mathbf{x})]$, computed for the 45 pairs of images of our ensemble.

Table 1
Cross-correlation coefficient between the mean $\langle I(\mathbf{x})\rangle$ and standard deviation std$[I(\mathbf{x})]$ computed for the 45 pairs of luminance and depth images of our ensemble.

		Luminance	
		Mean	St. dev.
Depth	Mean	−0.18	−0.23
	St. dev.	−0.17	−0.08

to examine how the scaling properties evolve and how their quantitative parameters relate to the typology of the images [54]. One could think of various homogeneous categories of outdoor or indoor scenes, or even underwater scenes. Various fractal parameters could then be envisaged to serve for instance to image indexing in large databases. However, the ensembles of outdoor natural scenes with woods, bushes and plants as studied here, are specially important since they have formed for a long period of time the environment in which the visual system has evolved and developed [16–18], and in this respect their (scale-invariant) statistics carry specific relevance. In this sense, the visual system and its remarkable properties for image processing may have been optimized for/by the statistics of natural images; and better knowledge of these complex statistics, including their fractal aspects, is a guide for better understanding of vision.

Also, natural structures like leaves, plants and trees are known to incorporate fractal arrangements of their own in their three-dimensional constitution [55–57]. A further study could be to specifically investigate how the fractal properties observed in depth and luminance images relate or give access to such three-dimensional constitutive fractal properties of plants.

In the present study we did not make any assumption on a possible dependence between luminance and depth images. Instead, we implemented direct analysis of the statistics of the luminance and the depth images and their scaling behaviors, offering useful independent references. The separate statistical analyses revealed fractal scale invariances present simultaneously in the luminance and in the depth images, together with generally weak statistical correlation between the two types of images. These scale invariances measured here simultaneously and independently in the luminance and in the depth images, although distinct in their quantitative detail, may however suggest the possibility of some dependence existing at a higher level between these two types of images. Analysis of statistical dependence between the scaling in luminance and depth images could in this respect be interesting to prolong, to better understand how luminance information and the way it spatially distributes over an image can carry information about depth and the three-dimensional organization of a physical scene [58,51,52]. This could provide cues to the visual system for depth reconstruction or inference from luminance. However, as we have seen, a simple measure like the cross-correlation manifests only weak dependence between luminance and depth images. This in particular excludes simple linear relations to connect luminance and depth images. Some higher-order measures of statistical dependence may be necessary to better capture a possible relation, especially allowing one to connect the fractal scale-invariance properties common in luminance and in depth images. Measures like mutual information could be appropriate to explore, possibly a directed version of mutual information, in order to account for the reality that the depth images are usually not affected by the illumination conditions, while the luminance images may be significantly influenced by the depths in the scene yet in a way not adequately captured by a linear measure of dependence like the cross-correlation. Such informational measures could be useful to better assessment of the information of a physical scene that is conveyed in an image. Fractal properties seem to be a robust characteristics attached to images of natural scenes. Such fractal properties, common to several distinct types of images, could serve as a useful guide to define and follow the informational content in images, and this could be relevant to efficient strategies for visual perception and computational vision in a three-dimensional world.

Another direction where our study could carry useful significance is the analysis and modeling of the interaction of light with three-dimensional natural structures, especially those made of foliage, leaves. The depth images studied here measure the structure of the outer surface visible for the objects in a scene. This represents the surface that the scene presents to an incident external light. For natural scenes with plants and leafy foliage, this outer surface controls the interception of solar radiation by the foliage and is therefore important for subsequent metabolic and growth processes in the plant based on photosynthesis. Our analysis of depth images from natural scenes indicates that such outer surfaces from plants and foliage structures tend to display a fractal character. Such a fractal organization of their outer surface may be a feature contributing to high efficacy of plants for light interception. Several recent studies suggest the importance of the three-dimensional and multiscale organization of plants in efficient light interception [59–61]. The depth images and their association with luminance images as investigated here, can contribute to the analysis and modeling of these processes of light interaction and interception by plants. They offer possibilities of measurement and quantitative characterization in this domain. In particular, the fractal organization could represent an important feature, possibly manifesting distributed lacunarities to allow light penetration in the deep of the foliage, and spatial structures forming mazes or traps for enhancing light absorption, together realizing an efficient combination of diffusers and absorbers in three dimensions. Moreover, the three-dimensional arrangement of foliage, as probed by the depth images, and with fractal organization, could suggest interesting configurations to the technology of solar energy collectors. It is being realized that flat planar solar panels may not represent the most efficient configuration to collect solar energy [62,63]: they offer only one chance of interaction to the incident light before specular reflection, and are matched to only one direction of incidence if one wants to avoid active sun tracking. By contrast, three-dimensional structures, with abilities of light trapping and enhanced volume of interaction, are being recognized as promising alternatives for efficient solar collectors [62,63]. In this re-

spect, the foliage of plants could suggest interesting architectures for such solar collectors. The depth images investigated here precisely probe the structure of the outer surface which controls light interception. They reveal here a fractal organization which could be an interesting ingredient to test in the technology of solar collectors.

In this way, both the novel technological low-cost imaging sensor demonstrated here, and the depth images it delivers, together with the new fractal properties uncovered here, are connected to several interesting directions of development.

Acknowledgement

Yann CHÉNÉ acknowledges support from *Région Pays de la Loire*, France, for the funding of his Ph.D.

References

[1] O'Sullivan JA, Blahut RE, Snyder DL. Information-theoretic image formation. IEEE Trans Inform Theory 1998;44:2094–123.
[2] Párraga CA, Brelstaff G, Troscianko T, Moorehead IR. Color and luminance information in natural scenes. J Opt Soc Am A 1998;15:563–9.
[3] Chandler DM, Field DJ. Estimates of the information content and dimensionality of natural scenes from proximity distributions. J Opt Soc Am A 2007;24:922–41.
[4] Olshausen BA, Field DJ. Natural image statistics and efficient coding. Network: Comput Neural Syst 1996;7:333–9.
[5] Tanaka K. Statistical-mechanical approach to image processing. J Phys A 2002;35:R81–R150.
[6] Geisler WS. Visual perception and the statistical properties of natural scenes. Ann Rev Psychol 2008;59:167–92.
[7] Olshausen BA, Field DJ. Vision and the coding of natural images. Am Scient 2000;88:238–45.
[8] Srivastava A, Lee AB, Simoncelli EP, Zhu SC. On advances in statistical modeling of natural images. J Math Imaging Vis 2003;18:17–33.
[9] Karklin Y, Lewicki MS. Learning higher-order structures in natural images. Network: Comput Neural Syst 2003;14:483–99.
[10] Petrov Y, Zhaoping L. Local correlations, information redundancy and sufficient pixel depth in natural images. J Opt Soc Am A 2003;20:56–66.
[11] McDermott KC, Webster MA. Uniform color spaces and natural image statistics. J Opt Soc Am A 2012;29:182–7.
[12] Field DJ. Relations between the statistics of natural images and the response properties of cortical cells. J Opt Soc Am A 1987;4:2379–94.
[13] Webster MA, Mollon JD. Adaptation and the color statistics of natural images. Vis Res 1997;37:3283–98.
[14] Párraga CA, Troscianko T, Tolhurst DJ. The human visual system is optimised for processing the spatial information in natural visual images. Current Biol 2000;10:35–8.
[15] Simoncelli EP, Olshausen BA. Natural image statistics and neural representation. Ann Rev Neurosci 2001;24:1193–216.
[16] Regan BC, Julliot C, Simmen B, Vienot F, Charles-Dominique P, Mollon JD, et al. foliage and the evolution of primate colour vision. Philos Trans Roy Soc Lond B 2001;356:229–83.
[17] Balboa RM, Grzywacz NM. Power spectra and distribution of contrasts of natural images from different habitats. Vis Res 2003;43:2527–37.
[18] Tkacik G, Garrigan P, Ratliff C, Milcinski G, Klein JM, Seyfarth LH, et al. Natural images from the birthplace of the human eye. PLoS One 2011;6:1–12. e20409.
[19] Peli T. Multiscale fractal theory and object characterization. J Opt Soc Am A 1990;7:1101–12.
[20] Ruderman DL. Origins of scaling in natural images. Vis Res 1997;37:3385–98.
[21] Abedini MJ, Shaghaghian MR. Exploring scaling laws in surface topography. Chaos, Solitons Fract 2009;42:2373–83.
[22] Turiel A, Parga N, Ruderman DL, Cronin TW. Multiscaling and information content of natural color images. Phys Rev E 2000;62:1138–48.
[23] Ahammer H, Kroepfl JM, Hackl C, Sedivy R. Fractal dimension and image statistics of intraepithelial neoplasia. Chaos, Solitons Fract 2011;44:86–92.
[24] Burton GJ, Moorhead IR. Color and spatial structure in natural scenes. Appl Opt 1987;26:157–70.
[25] Tolhurst DJ, Tadmor Y, Chao T. Amplitude spectra of natural images. Ophthal Physiol Opt 1992;12:229–32.
[26] Ruderman DL, Bialek W. Statistics of natural images: Scaling in the woods. Phys Rev Lett 1994;73:814–7.
[27] Ruderman DL. The statistics of natural images. Network: Comput Neural Syst 1994;5:517–48.
[28] van der Schaaf A, van Hateren JH. Modelling the power spectra of natural images: statistics and information. Vis Res 1996;36:2759–70.
[29] Párraga CA, Tolhurst DJ. The effect of contrast randomisation on the discrimination of changes in the slopes of the amplitude spectra of natural scenes. Perception 2000;29:1101–16.
[30] Hsiao WH, Millane RP. Effects of occlusion, edges,and scaling on the power spectra of natural images. J Opt Soc Am A 2005;22:1789–97.
[31] Mastrolonardo M, Conte E, Zbilut JP. A fractal analysis of skin pigmented lesions using the novel tool of the variogram technique. Chaos, Solitons Fract 2006;28:1119–35.
[32] Dong DW, Atick JJ. Statistics of natural time-varying images. Network: Comput Neural Syst 1995;6:345–58.
[33] Chapeau-Blondeau F, Chauveau J, Rousseau D, Richard P. Fractal structure in the color distribution of natural images. Chaos, Solitons Fract 2009;42:472–82.
[34] Chauveau J, Rousseau D, Chapeau-Blondeau F. Fractal capacity dimension of three-dimensional histogram from color images. Multidimen Syst Signal Process 2010;21:197–211.
[35] Chauveau J, Rousseau D, Richard P, Chapeau-Blondeau F. Multifractal analysis of three-dimensional histogram from color images. Chaos, Solitons Fract 2010;43:57–67.
[36] Buades A, Lisani JL, Morel JM. Dimensionality of color space in natural images. J Opt Soc Am A 2011;28:203–9.
[37] Balboa RM, Tyler CW, Grzywacz NM. Occlusions contribute to scaling in natural images. Vis Res 2001;41:955–64.
[38] Pesquet-Popescu B, Lévy Véhel J. Stochastic fractal models for image processing. IEEE Signal Process Mag 2002;19(5):48–62.
[39] Gousseau Y, Roueff F. Modeling occlusion and scaling in natural images. SIAM J Multiscale Model Simulat 2007;6:105–34.
[40] Chainais P. Infinitely divisible cascades to model the statistics of natural images. IEEE Trans Pattern Anal Mach Intell 2007;29:2105–19.
[41] Dal Mutto C, Zanuttigh P, Cortelazzo GM. Time-of-Flight Cameras and Microsoft Kinect. New York: Springer; 2012.
[42] Gonzalez-Sanchez T, Puig D. Real-time body gesture recognition using depth camera. Electron Lett 2011;53:697–8.
[43] Chang YJ, Chen SF, Huang JD. A Kinect-based system for physical rehabilitation: A pilot study for young adults with motor disabilities. Res Develop Disabil 2011;32:2566–70.
[44] Chéné Y, Rousseau D, Lucidarme P, Bertheloot J, Caffier V, Morel P, et al. On the use of depth camera for 3D phenotyping of entire plants. Comput Electron Agric 2012;82:122–7.
[45] Schwarz LA, Mkhitaryan A, Mateus D, Navab N. Human skeleton tracking from depth data using geodesic distances and optical flow. Image Vision Comput 2012;30:217–26.
[46] Dutta T. Evaluation of the Kinect sensor for 3-D kinematic measurement in the workplace. Appl Ergon 2012;43:645–9.
[47] Hernández-López JJ, Quintanilla-Olvera AL, López-Ramírez JL, Rangel-Butanda FJ, Ibarra-Manzano MA, Almanza-Ojeda DL. Detecting objects using color and depth segmentation with Kinect sensor. Proc Technol 2012;3:196–204.
[48] Khoshelham K, Oude Elberink SJ. Accuracy and resolution of Kinect depth data for indoor mapping applications. Sensors 2012;12:1437–54.
[49] Maimone A, Bidwell J, Peng K, Fuchs H. Enhanced personal autostereoscopic telepresence system using commodity depth cameras. Comput Graph 2012;36:791–807.
[50] Howe CQ, Purves D. Range image statistics can explain the anomalous perception of length. Proc Nat Acad Sci USA 2002;99:13184–8.
[51] Potetz B, Lee TS. Statistical correlations between two-dimensional images and three-dimensional structures in natural scenes. J Opt Soc Am A 2003;20:1292–303.
[52] Potetz B, Lee TS. Scaling laws in natural scenes and the inference of 3D shape. In: Weiss Y, Schölkopf B, Platt J, editors. Advances in Neural Information Processing Systems, vol. 18. Cambridge: MIT Press; 2006. p. 1089–96.

[53] Potetz B, Lee TS. Scene statistics and 3D surface perception. In: Tyler CW, editor. Computational Vision: From Surfaces to Objects. Boca Raton, FL: Chapman & Hall; 2010. p. 1–25 (Chapter 1).
[54] Torralba A, Oliva A. Statistics of natural image categories. Network: Comput Neural Syst 2003;14:391–412.
[55] Critten DL. Fractal dimension relationships and values associated with certain plant canopies. J Agric Eng Res 1997;67:61–72.
[56] Martinez Bruno O, de Oliveira Plotze R, Falvo M, de Castro M. Fractal dimension applied to plant identification. Inform Sci 2008;178:2722–33.
[57] Chandra M, Rani M. Categorization of fractal plants. Chaos, Solitons Fract 2009;41:1442–7.
[58] Torralba A, Oliva A. Depth estimation from image structure. IEEE Trans Pattern Anal Mach Intell 2002;24:1226–38.
[59] Da Silva D, Boudon F, Godin C, Sinoquet H. Multiscale framework for modeling and analyzing light interception by trees. Multiscale Model Simulat 2008;7:910–33.
[60] Parveaud CE, Chopard J, Dauzat J, Courbaud B, Auclair D. Modelling foliage characteristics in 3D tree crowns: Influence on light interception and leaf irradiance. Trees 2008;22:87–104.
[61] Munier-Jolain NM, Guyot SHM, Colbach N. A 3D model for light interception in heterogeneous crop: Weed canopies: model structure and evaluation. Ecol Modell 2013;250:101–10.
[62] Myers B, Bernardi M, Grossman JC. Three-dimensional photovoltaics. Appl Phys Lett 2010;96:071902,1.
[63] Bernardi M, Ferralis N, Wan JH, Villalon R, Grossman JC. Solar energy generation in three dimensions. Energy Environ Sci 2012;5:6880–4.